Materials Science & Engineering A 807 (2021) 140845

Contents lists available at ScienceDirect

Materials Science & Engineering A

journal homepage: http://www.elsevier.com/locate/msea

Unveiling damage sites and fracture path in laser powder bed fusion AlSi10Mg: Comparison between horizontal and vertical loading directions

Lv Zhao [a,b,d,*], Juan Guillermo Santos Macías [b], Thierry Douillard [c], Zhenhuan Li [a,d], Aude Simar [b]

[a] Department of Mechanics, School of Aerospace Engineering, Huazhong University of Science and Technology, Wuhan, China
[b] Institute of Mechanics, Materials and Civil Engineering, UCLouvain, Louvain-la-Neuve, Belgium
[c] Université de Lyon, Mateis, INSA Lyon, UMR5510 CNRS, Villeurbanne, France
[d] Hubei Key Laboratory of Engineering Structural Analysis and Safety Assessment, 1037 Luoyu Road, Wuhan, China

ARTICLE INFO

Keywords:
Laser powder bed fusion
AlSi10Mg
Microstructure
Damage
Fracture path

ABSTRACT

The laser powder bed fusion (LPBF) additively manufactured AlSi10Mg alloy has been subjected to numerous investigations addressing its microstructure and mechanical properties. However, there is still a gap in the understanding of the correlation between the microstructure and fracture behavior, in particular when the melt pool border is oriented differently to tensile load. In this work, damage nucleation sites and fracture path of as built LPBF AlSi10Mg were analyzed and compared for two loading directions. For the first time, the orientation of the melt pool border is shown to present negligible effect on a ductility exceeding 10%, in contrast to previous works. Through observation and statistical analysis of damage, it is found for both loading directions that the melt pool border does not exhibit damage localization. When the melt pool border is perpendicular to tensile load, the crack propagates frequently along the coarse melt pool due to easier damage growth in this relatively softer region. Nevertheless, the ductility is barely compromised owing to delayed damage coalescence across larger α-Al cells.

1. Introduction

Laser powder bed fusion (LPBF) metals are promising for structural components involving complex geometry, presenting high potential for applications in aerospace, automotive and biomedical industries. Due to extremely large thermal gradient and cooling rate, LPBF metals generally exhibit very fine microstructure which leads to higher mechanical strength compared to their counterparts produced by traditional methods, such as casting and powder metallurgy [1–3].

Among the most commonly studied LPBF metals, AlSi10Mg stands out owing to its high strength-to-density ratio and good corrosion resistance [4]. LPBF AlSi10Mg has been investigated for more than ten years, and knowledge on its characteristic microstructure, defects, mechanical strength and resistance to fatigue has been well established [4,5]. The layer-by-layer manufacturing strategy of the LPBF process generally produces melt pool structures, with partial remelting of the previously solidified material when building the ongoing layer. Owing to epitaxial growth under directed solidification, (100) texture along building direction is generally observed in LPBF Al alloys [6,7]. Moreover, the microstructure of LPBF AlSi10Mg presents variations in different regions of the melt pool. According to the morphology and size of the Si-rich eutectic phase, the melt pool is commonly divided into fine melt pool (FMP) zone, coarse melt pool (CMP) zone and heat affected zone (HAZ) [8]. The CMP and HAZ are generally considered to form the melt pool border, which occupies a much smaller melt pool volume compared to the FMP zone [9–11]. Through focused ion beam/scanning electron microscopy (FIB/SEM) tomography data, it has recently been shown that the Si-rich phase manifests a 3D interconnected morphology with an extremely high connectivity in the FMP (0.99) and CMP (0.85), while the 3D network is degraded and presents a relatively low connectivity (around 0.1) in the HAZ [11]. Note that connectivity is defined as the volume fraction of the largest object of one phase with respect to the total volume fraction of that phase in the analyzed volume. Object represents here an individual continuous 3D region of the analyzed phase. This definition has been widely used in the analysis of interconnected secondary phases [12,13].

The difference in Si-rich phase morphology was considered to account for hardness variation between zones, i.e., the FMP being the

* Corresponding author. Department of Mechanics, School of Aerospace Engineering, Huazhong University of Science and Technology, Wuhan, China.
E-mail address: lvzhao@hust.edu.cn (L. Zhao).

https://doi.org/10.1016/j.msea.2021.140845
Received 4 December 2020; Received in revised form 21 January 2021; Accepted 25 January 2021
Available online 3 February 2021

Table 1
Mechanical properties of LPBF AlSi10Mg reported in literature. RT denotes room temperature. The mechanical properties are the average values reported in the corresponding references.

Laser power (W)	Scan speed (mm/s)	Layer thickness (μm)	Hatch spacing (μm)	Scan strategy	Platform temperature (°C)	Specimen orientation	Yield strength (MPa)	Tensile strength (MPa)	Elongation to fracture (%)	Ref.
960	>1000	50	200	–	RT	**Horizontal**	232	415	8.0	[25]
						Vertical	204	437	5.5	
					220	**Horizontal**	130	250	6.4	
						Vertical	150	305	4.0	
380	1000	30	100	67° rotation	RT	**Horizontal**	280	472	7.8	[26]
						Vertical	230	475	5.6	
370	1300	30	190	67° rotation	80	**Horizontal**	264	451	8.6	[3]
						Vertical	247	482	6.5	
350	1650	30	130	–	150	**Horizontal**	270	450	6.6	[15]
						Vertical	260	460	5.2	
350	1150	50	170	Stripes	150	**Horizontal**	288	414	5.6	[27]
						Vertical	271	419	4.1	
370	1300	30	130	67° rotation	165	**Horizontal**	269	418	7.8	[28]
						Vertical	226	429	4.0	
340	1300	30	200	67° rotation	160	**Horizontal**	248	386	10.6	[29]
						Vertical	228	412	7.0	
370	1300	30	190	67° rotation	200	**Horizontal**	235	386	7.2	[16]
						Vertical	210	392	5.5	
370	1300	30	190	67° rotation	300	**Horizontal**	–	338	4.6	[30]
						Vertical	–	366	4.4	
350	930	50	420	90° rotation	200	**Horizontal**	241	399	6.5	[31]
						Vertical	209	357	3.2	
350	1150	50	170	67° rotation	200	**Horizontal**	225	364	6.5	[32]
						Vertical	205	377	3.3	
300	1650	30	130	67° rotation	200	**Horizontal**	265	440	4.7	[33]
						Vertical	284	438	2.8	
400	1000	25	175	Island	–	**Horizontal**	–	358	7.4	[34]
						Vertical	–	334	3.6	
175	1025	30	97.5	Island	–	**Horizontal**	233	370	4.9	[22]
						Vertical	211	272	1.7	

strongest and the HAZ being the weakest, as revealed by nano-indentation tests [8,14]. Moreover, LPBF AlSi10Mg exhibits anisotropic mechanical properties [14], which, according to Xiong et al. [9], are mainly induced by the melt pool orientation, while texture along the building direction has little effect. In general, the material was found to present lower elongation to failure when it was loaded along the building direction (i.e., vertical loading) [3,15,16], where the melt pool border was expected to experience strain localization due to its lower strength [17]. Although attempts have been made to correlate the strengthening mechanism with the microstructural characteristics, most studies only addressed the FMP zone [11,16,18], leaving the melt pool border aside. Moreover, different mechanisms were proposed to evaluate the strengthening effect of the Si-rich eutectic phase. Early investigations only considered the Hall-Petch like [16] or Orowan [2] effect; recent studies take into account the load bearing contribution [11,18], as supported by experimental assessments revealing much higher stress in the Si-rich phase [19] and very high density of geometrically necessary dislocations (GND) near the Al/Si interface [18,20]. Therefore, accurate assessment and implementation of the strain partition throughout the melt pool structure are still to be achieved.

Fracture of metallic materials is generally assisted by strain localization involving either plastic instability or void growth and coalescence, determining the ductility of the material [21]. Table 1 evidences a quite large scattering of elongation to fracture of LPBF AlSi10Mg reported in literature, for both horizontal and vertical specimens. The primary cause for this large scattering could be the various LPBF process parameters, which resulted in different levels of defects and microstructure heterogeneity. Specifically, low laser power was found to lead to large and sharp lack of fusion porosity [22,23]. According to Hirata et al. [24], the elongation of LPBF AlSi10Mg was strongly reduced by large and dense porosity due to insufficient energy density, which could explain the very low ductility of parts built with low laser power (see the properties of ref. [22] of Table 1). When comparing the mechanical performance between horizontal and vertical specimens built with identical parameters, i.e., containing close porosity level, the elongation of vertical specimens was generally lower, often quite significantly.

The lower elongation to fracture of vertical specimens was widely considered to result from strain localization and crack propagation through the CMP [9,15,26,35], or the HAZ [8]. However, this conjecture should be applied with caution. First, vertical specimens were found to generally present similar or even higher tensile strength compared to

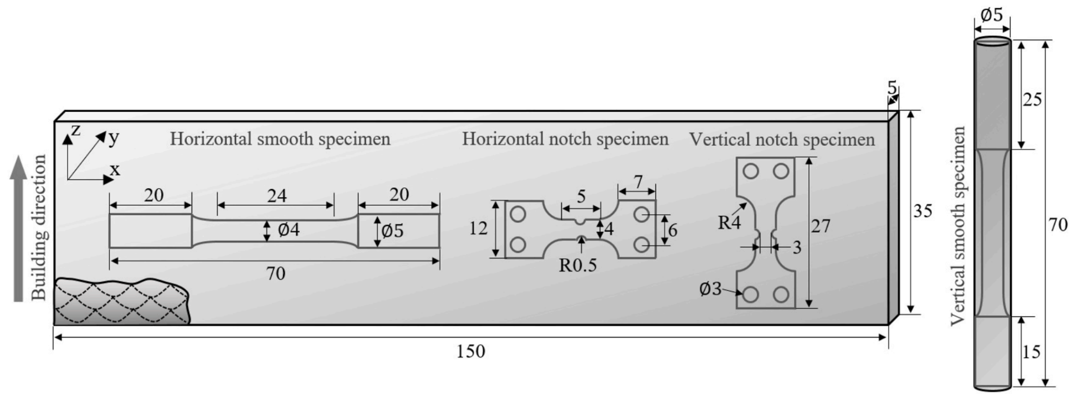

Fig. 1. Geometry and dimension of as built LPBF AlSi10Mg sample as well as extracted tensile specimens.

Table 2
Chemical composition in wt.% of the LPBF AlSi10Mg sample.

	Al	Si	Mg	Fe
LPBF AlSi10Mg	Bal.	9.68	0.43	0.13

horizontal specimens (see Table 1). In this sense, the fracture strain of vertical specimens could be limited by high flow stress due to the strength-ductility trade-off [26,36]. Second, it is worth mentioning that most studies only reported the elongation to failure (engineering strain), which is not intrinsic to the material and cannot reflect the true ductility when necking is involved. Moreover, the effect of gradient in microstructure along the building direction, as shown in [37,38], was rarely discussed in the analysis of ductility of vertical specimens. Indeed, Hitzler et al. [31] reported that fracture mostly took place towards the upper end of the built specimens, where the hardness was found to be smaller than that for the lower portion (closer to build platform). In addition, the morphology of initial porosity could also be partly responsible for the lower fracture strain of vertical specimens [17], as large porosity was found to be flat and lie along melt pool borders due to lack of fusion when using a relatively low laser energy [22,39]. Therefore, the origin for the lower ductility (if present) of vertical specimens should be clarified case-by-case, as there is no apparent relationship between the parameters and the properties. In other words, the effect of the softer melt pool border (i.e., CMP and HAZ) on ductility should be assessed after excluding other influencing factors mentioned above.

The present work aims at addressing ductility and damage mechanism of LPBF AlSi10Mg in both horizontal and vertical directions, excluding the effect of gradient in microstructure and porosity. Particular attention was paid to the 3D morphology of the Si-rich phase across the melt pool border. The ductility, defined as true strain at fracture, was measured from uniaxial tensile tests. The damage nucleation sites and fracture path were carefully assessed with post-mortem observations. Moreover, damage statistics in different zones were obtained to understand the failure mechanism. Finally, the effect of the orientation of the melt pool border on ductility was discussed.

2. Materials and experiments

2.1. Material manufacturing

The studied LPBF AlSi10Mg sample was manufactured with an EOS M290 machine using the machine manufacturer suggested parameters "AlSi10Mg_Speed 1.0" [40] which set the laser power to 390 W, the layer thickness to 30 μm, the scan speed to 1300 mm/s and the hatch spacing to 0.19 mm. The scan direction rotated 67° between layers. The build platform temperature was 35 °C. The powder used for the LPBF presents an average equivalent diameter of approximately 25 μm. Two types of samples were manufactured, one presents a plate shape which is 150 mm in length, 35 mm in width and 5 mm in thickness, the other presents a cylinder shape which is 70 mm in length and 5 mm in diameter (see Fig. 1). The plate samples were used for microstructure characterization, uniaxial tensile tests of horizontal specimens and double notched tensile tests, the cylinder samples were used for uniaxial tensile tests of vertical specimens.

The chemical compositions of the built samples were measured by inductively coupled plasma optical emission spectroscopy (ICP-OES) and are given in Table 2.

2.2. Microstructure characterization

To characterize the microstructure of the as built sample, metallurgical polishing was performed, followed by chemical etching using 0.5 vol.% HF solution to enhance the phase contrast. The two-dimensional (2D) microstructural features were observed with optical microscopy and scanning electron microscopy (SEM). To reveal the three-dimensional (3D) morphology of the Si-rich phase, especially at the melt pool border, layers of material were locally peeled off the sample with focused ion beam (FIB). An SEM micrograph was acquired prior to every subsequent peeling-off to record the microstructure as a slice, then the slices were reconstructed to obtain the 3D volume. The voxel size of the volume is 5 nm, allowing to probe the typical fine microstructure of LPBF AlSi10Mg. More details of the FIB/SEM tomography experiment are given by Santos Macías et al. [11]. The data processing was performed with the ImageJ software, different objects were colored differently via a Matlab script.

2.3. Mechanical properties testing

Uniaxial tensile tests were performed with smooth round bars depicted in Fig. 1. These specimens were machined from the as built samples by electron discharge machining (EDM) and lathe. In order to avoid any eventual microstructure gradient induced strain localization as revealed by Hitzler et al. [31], the gripping head close to the build platform was intentionally made shorter than the other for the vertical specimens (see Fig. 1). The total length and the gauge dimension of the specimens are identical between the two loading directions. Double notched tensile testing (Fig. 1) was also performed to investigate the fracture behavior. Both horizontal and vertical specimens were tested for comparison, presenting identical geometry and size. To avoid the effect of microstructure gradient on damage, the notch filament was located at similar height along the building directions, as illustrated in Fig. 1. The uniaxial tensile tests were carried out with a Zwick tensile machine, using a 20 mm gauge length extensometer for strain measurement. The crosshead displacement rate was 1 mm/min. At least four specimens were tested to obtain the representative mechanical strength and ductility. The double notched tensile tests were carried out using a

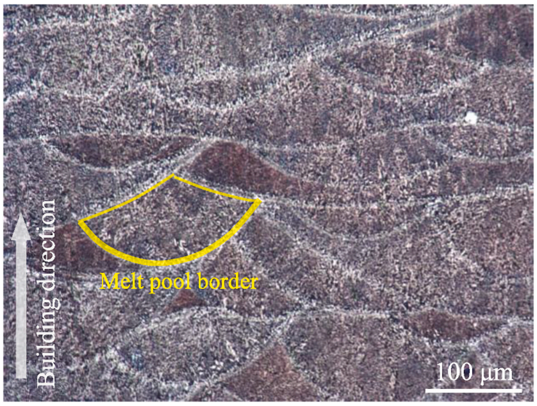

Fig. 2. Observation of melt pool structure.

Gatan microtest tensile stage. The crosshead displacement rate was 0.1 mm/min. Two tests were performed, one inside the SEM, for each condition.

After fracture, the morphology of the fracture surface was observed with SEM. Moreover, the broken specimens were polished to the mid-thickness plane to reveal the damage feature and fracture path in relation to the microstructure. These observations also allow obtaining damage statistics in different zones of the melt pool.

3. Results

3.1. Microstructure

The cross-section of the melt pool structure was observed under optical microscope, see Fig. 2. The shape of the melt pool can be well distinguished due to the presence of the melt pool border. The melt pool has a width of approximately 180 μm and a height of 60 μm. From Fig. 2, it can be seen that the melt pool border occupies a very small volume of the melt pool.

Zooming in on the melt pool, the fine microstructure composed of α-Al and Si-rich eutectic phase is observed in the 2D SEM micrograph (Fig. 3). Fig. 3a presents the structure across a melt pool border. The Si-rich eutectic phase manifests as an interconnected network in the CMP and FMP, which appears to be broken down in the HAZ. The enclosed Al cells contain extremely fine Si-rich particles that present a diameter in the order of 10 nm (Fig. 3b and c). The CMP and HAZ constitute the melt pool border that presents a thickness of approximately 7 μm. The FMP, occupying most of the material volume and being the most representative microstructure, is observed at different cross-sectional planes. At the plane parallel to the building direction, the Si-rich phase presents an elongated shape following epitaxial grain growth (Fig. 3b), while at the plane perpendicular to the building direction, an equiaxial morphology is observed (Fig. 3c). This morphology indicates that the Si-rich phase has a polyhedral shape composed of platelets, as recently confirmed by Santos Macías et al. [11]. Based on this morphology, the Si-rich eutectic structure unit is schematized in Fig. 3d. This sketch corresponds well to the planar view of the Si-rich phase in both xz (Fig. 3e) and xy (Fig. 3f)

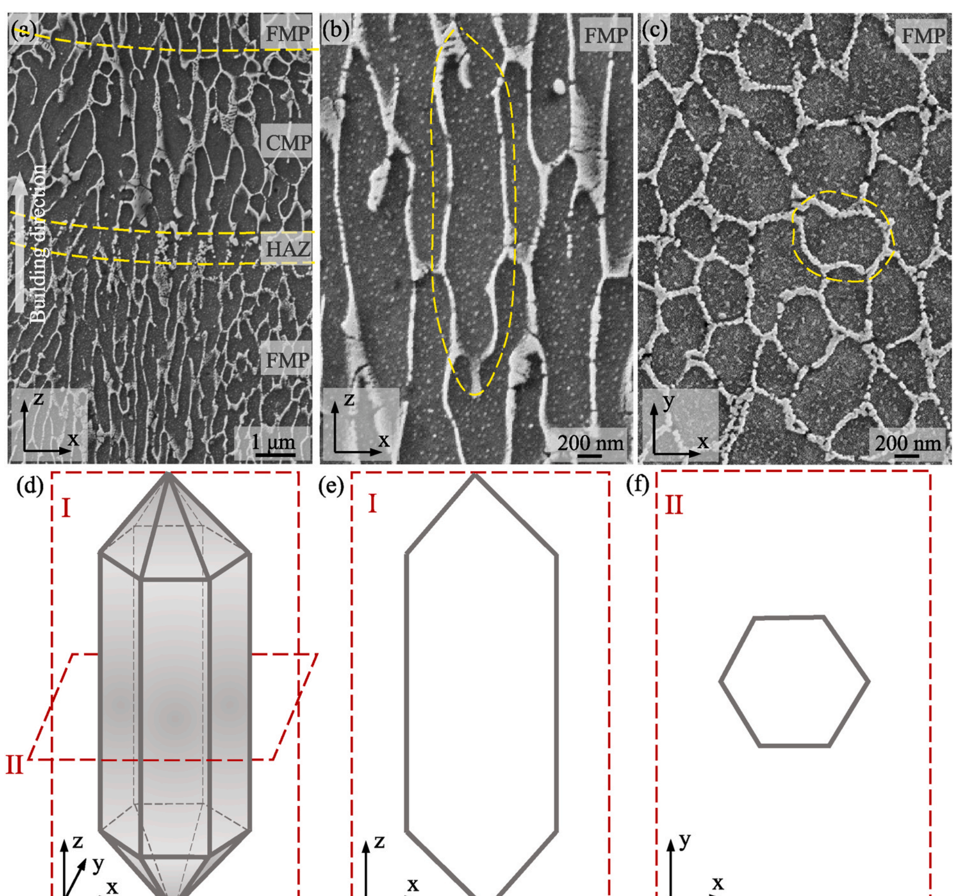

Fig. 3. Melt pool structure with distinctive regions, i.e., fine melt pool (FMP), coarse melt pool (CMP) and heat affected zone (HAZ) at the melt pool border (a), 2D morphology of the FMP Si-rich eutectic network at xz (b) and xy planes (c); schematic Si-rich eutectic network structure (d) and its 2D representation on different cut planes (e)–(f).

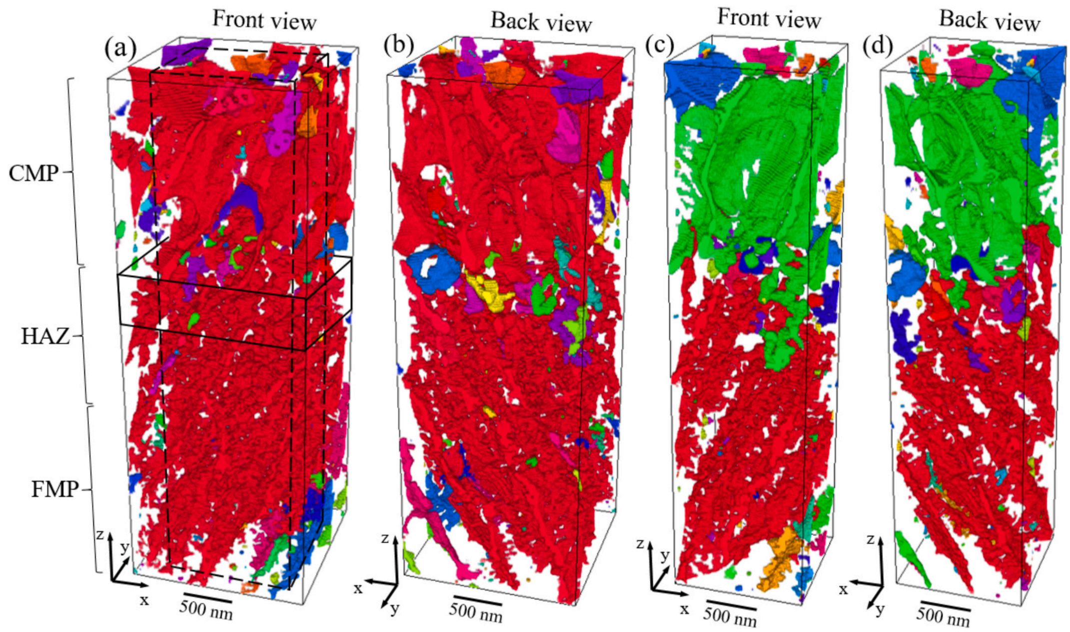

Fig. 4. 3D visualization of the Si-rich eutectic structure at a melt pool border. The block size of (a) and (b) is 1750 × 1750 × 5000 nm (front and back view, respectively). The volume of (c) (and (d)) is sub-volume of (a) and has a size of 1250 × 1250 × 5000 nm. Different colors are used to distinguish disconnected objects using the voxel connectivity criterion of first 6 neighbors. The solid parallelepiped in (a) is to mark the position of Fig. 5a. (For interpretation of the references to color in this figure legend, the reader is referred to the Web version of this article.)

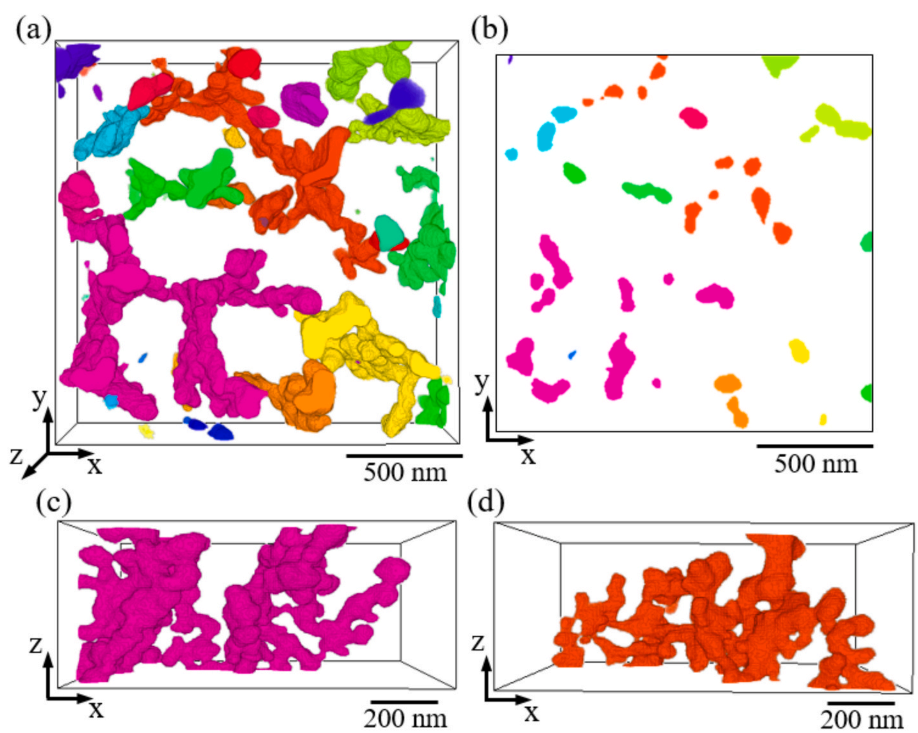

Fig. 5. 3D visualization of the Si-rich eutectic structure of the HAZ extracted from the volume of Fig. 4a (solid parallelepiped of 1750 × 1750 × 505 nm) (a), the slice near the center (z = 265 nm) (b), the morphology of the largest (c) and the second largest (d) Si-rich phase of (a). The objects are distinguished with different colors. (For interpretation of the references to color in this figure legend, the reader is referred to the Web version of this article.)

planes.

According to the 2D SEM observation, the Si-rich eutectic network significantly disintegrates in the HAZ. However, 2D characterization might be insufficient given the complex microstructure of LPBF AlSi10Mg. Therefore, FIB/SEM tomography has been performed to provide a 3D visualization of the microstructure, using a voxel size of 5 nm. Fig. 4 allows to assess the features, especially the connectivity of the Si-rich phase in the melt pool border region. Each color of Fig. 4 represents a disconnected object (the Si-rich phase) defined using the voxel connectivity criterion of 6 first neighbors. The explanation of the voxel connectivity criterion can be found in Supplementary Fig. S1. Note that Fig. 4b and d corresponds to the back view of Fig. 4a and c, respectively,

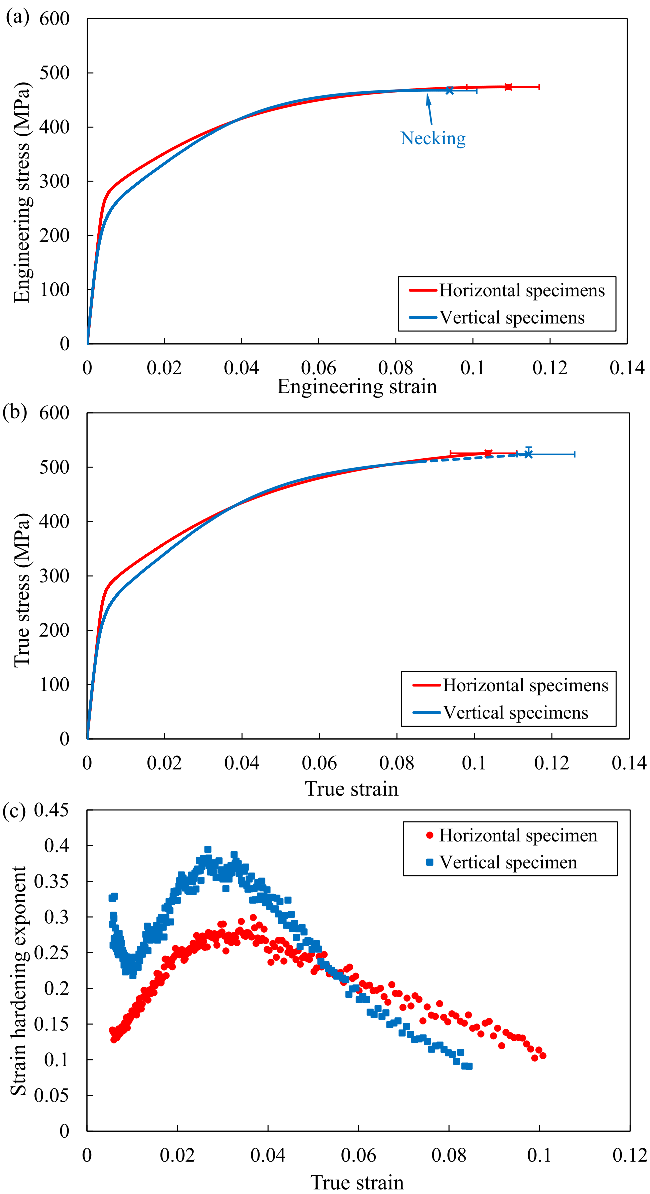

Fig. 6. Results of uniaxial tensile tests. Engineering stress-strain curves (a), true stress-strain curves (b), evolution of the strain hardening exponent (c). The error bars correspond to the lowest and highest stresses and strains at failure of the tested specimens. A linear extrapolation links the end of the true stress-true strain curve to the failure point to show the post-necking behaviour.

Table 3
Test results of notched tensile specimens. The failure stress is calculated with the initial thickness and ligament length. The displacement at failure is presented for comparison of ductility.

	Failure stress (MPa)	Displacement at failure (mm)
Notch horizontal	455±2	0.45±0.03
Notch vertical	461±6	0.48±0.01

for a more comprehensive presentation of the 3D visualization. Interestingly, it is observed that the CMP and FMP are well interconnected when analyzing a relatively big volume (1750 × 1750 × 5000 nm), as can be seen in Fig. 4a-b. However, when dealing with a smaller volume (1250 × 1250 × 5000 nm) extracted from the center of the aforementioned one (see the dashed box in Fig. 4a), the networks of the CMP and FMP are separated, as shown in Fig. 4c-d. Sub-volumes extracted from other positions (for example the four corners) are provided in Supplementary Fig. S2, confirming that the CMP and FMP are mostly disconnected at small scale. In other words, the interconnection between CMP and FMP observed in the larger volume (Fig. 4a) is achieved through local network interconnection (Supplementary Fig. S2b). It is also worth mentioning that when considering interconnection in such 3D volumes, the Si-rich phases in the HAZ are not fragmented enough to be singled out as individual objects, in contrast to 2D observations. Note that the blue, green and yellow objects seen at mid height of Fig. 4b do not constitute a region traversing the volume (in the y direction), as can be seen in the front view (Fig. 4a). They are more likely part of other Si-rich networks that are not included in the displayed 3D volume. These observations bring about two indications: first, the CMP and FMP zones present a connection at large scale, which breaks down at small scale; second, the HAZ cannot be well defined from the 3D microstructure, it appears to be part of the FMP.

What induces this significant difference between the 2D and 3D characterizations? In fact, the Si-rich eutectic network is composed of platelets in the FMP far from the melt pool border, as revealed by Santos Macías et al. [11]. However, the plate-like Si eutectic phase degrades to a branched morphology in the typical HAZ observed in the 2D micrograph, as clearly shown in Fig. 5a, c and d. It should be noted that the volume of Fig. 5 corresponds to the part right below the CMP (marked by the solid parallelepiped in Fig. 4a), i.e., the HAZ region. This particular shape can mislead the connectivity analysis in the 2D characterization. If one observes the 2D section of the Si-rich phase, it would be considered to be completely disconnected, as clearly evidenced in Fig. 5b. However, many of these 2D "globular particles" are in fact interconnected in 3D, as can be seen from the color representation of Fig. 5a and b, although the connectivity is lower compared to the FMP and CMP. Note that the connectivity of the Si-rich phase is 0.32 in this specific volume, while it is 0.99 and 0.85 for the FMP and CMP, respectively [11].

The Si-rich phase differs not only in morphology in different zones of the melt pool, but also in size. The Si-rich phase size in each zone has been properly characterized in a recent work [11] for the LPBF AlSi10Mg sample manufactured with the same machine and the same parameters. The thickness of the Si-rich phase of the FMP, CMP and HAZ is 50 nm, 70 nm and 90 nm, respectively.

In summary, the Si-rich phase presents a more complex structure than what can be observed in 2D SEM. The HAZ cannot be accurately characterized in 2D due to the branched morphology of the Si-rich phase. The Si-rich phase exhibits the highest interconnectivity and the smallest size in the FMP, the lowest interconnectivity and the largest size in the HAZ. The CMP stands out for high connection level and large Si-rich phase.

3.2. Mechanical strength and ductility

The results of the uniaxial tensile tests are provided in Fig. 6. Both engineering (Fig. 6a) and true (Fig. 6b) stress-strain curves are presented, accompanied with the evolution of the strain hardening exponent (Fig. 6c) calculated by $\varepsilon \cdot d\sigma_{fl}/(\sigma_{fl} \cdot d\varepsilon)$ where σ_{fl} denotes the flow stress. It should be noted that the specimens were broken randomly inside the extensometer gauge, indicating that the mechanical behavior was not affected by any gradient in microstructure. The yield strength of the vertical specimens is lower than that of the horizontal ones. However, their strain hardening exponent is higher at the early stage of plastic deformation, which drives the flow stress to overtake that of the horizontal specimens; it then decreases rapidly and falls below the strain hardening exponent of the horizontal specimens (Fig. 6c). In the end, the fracture stress is very close for the two loading directions (see Fig. 6b).

The horizontal specimens present higher elongation to failure (Fig. 6a), which is in line with previous reports in literature. However, the true fracture strain is found to be almost identical for the two loading

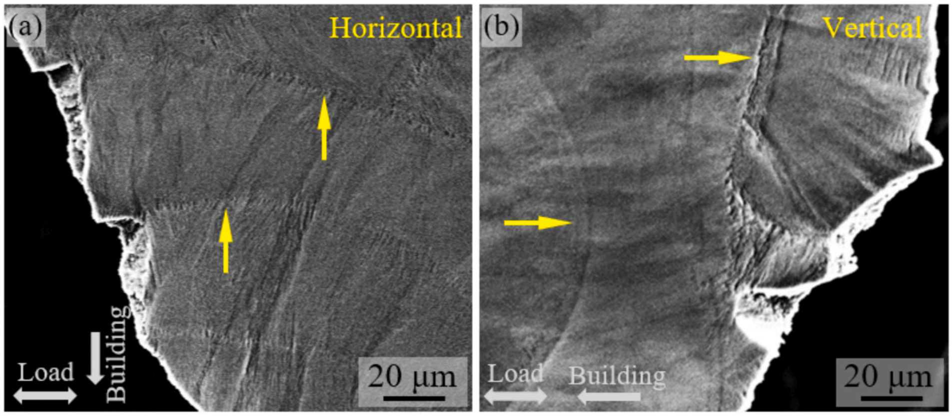

Fig. 7. Deformed microstructure near the crack of horizontal (a) and vertical (b) specimens. The yellow arrows point to regions of strain localization at the melt pool border. (For interpretation of the references to color in this figure legend, the reader is referred to the Web version of this article.)

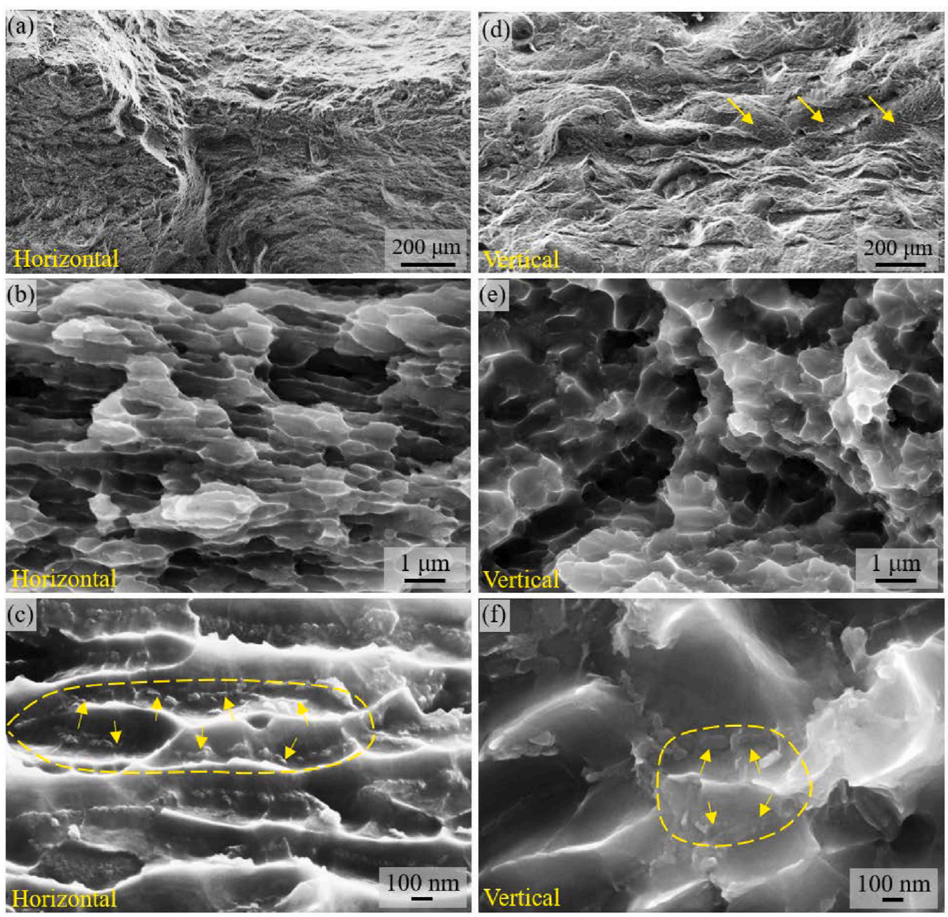

Fig. 8. Fracture surface morphology. Observation at different magnifications for the horizontal (a)–(c) and vertical (d)–(f) notched specimens. The arrows in (d) mark the traces of the melt pool border. The arrows in (c) and (f) point out the Si-rich eutectic phase on the fracture surface. The dashed enclosing lines indicate the Si-rich eutectic network.

directions. This indicates that the use of engineering strain obscures the true nature of the material ductility due to the necking of the vertical specimens. Note that the true fracture strain was calculated with $\varepsilon_f = ln(A_0/A_f)$ for vertical specimens because they involved post-necking deformation. The horizontal specimens were broken when the Considere's criterion was reached, so there is barely any macroscopic strain localization and the fracture strain is taken as the uniform strain measured with the extensometer. It is noteworthy that the material contains relatively low initial porosity, presenting no marked anisotropy or large flat lack of fusion pores, as shown in a previous work on the same material manufactured with the same machine and processing parameters [41]. Moreover, Zhao et al. [42] demonstrated that a low initial porosity does not present a significant impact on ductility of LPBF AlSi10Mg. Therefore, the ductility obtained in the present work should have a close correlation with the Si-rich network structure and connectivity, as will be addressed in the following section.

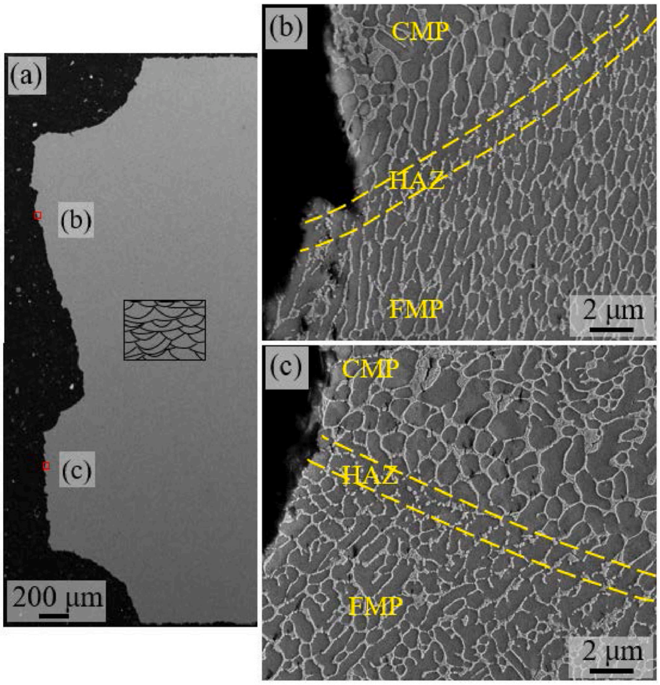

Fig. 9. Fracture path in the horizontal notched specimen. Overall observation (a), fracture path in relation to melt pool zone (b)–(c). The yellow dashed lines delimit the FMP, CMP and HAZ in (b)–(c). (For interpretation of the references to color in this figure legend, the reader is referred to the Web version of this article.)

3.3. Damage and fracture path

3.3.1. Double notched tensile testing

The fracture behavior and damage mechanism are analyzed based on the flat notched specimens (Fig. 1). The test results are presented in Table 3. Due to the notch sensitivity, the failure stress of the notched specimens is lower than that of the smooth specimens (472±2 MPa and 469±3 MPa for the horizontal and vertical smooth specimens, respectively). Given that the inter-notch ligament of both horizontal and vertical specimens is located at similar level along the building direction (see Fig. 1), the damage and fracture path are only affected by the orientation of the melt pool.

Both failure stress and global extension are very close for the horizontal and vertical notched specimens, coinciding with the results of the uniaxial tensile tests. In turn, it confirms that the comparison of mechanical strength and ductility obtained from the uniaxial tensile testing is not biased by the fact that the horizontal smooth bars are machined from plates while the vertical ones from cylinders (see Fig. 1).

For the tests conducted inside the SEM, the deformed microstructure near the crack is observed (Fig. 7). Strain localization at the melt pool border (see the arrows in Fig. 7a and b) can be seen for both loading directions. This is in line with the higher dislocation density at the melt pool border shown by Ben et al. [17], in particular for the vertical direction. Indeed, the Si-rich eutectic phase of the HAZ exhibits a lower connectivity (Fig. 5), and the Si-rich eutectic network of the CMP is coarser (Fig. 3a), both zones block less effectively dislocation motion compared to the FMP, thus leading to lower mechanical strength and producing strain localization at the melt pool border.

3.3.2. Fracture surface

The representative fracture surface morphology of the notched specimens resulting from the two loading directions is shown in Fig. 8. Some traces of the melt pool border can be observed for the vertical specimen (marked with the arrows in Fig. 8d), which is not the case for the horizontal one (Fig. 8a). At meso-scale, it is found that the horizontal specimen typically exhibits elongated lamellar morphology (Fig. 8b) while the vertical one presents hill-like morphology (Fig. 8e). When zooming in to study submicron details of the fracture surface, the Si-rich phase is observed, as indicated by the arrows in Fig. 8c and f. It is noteworthy that the Si-rich phase seen on the fracture surface is reminiscent of its morphology shown by the SEM micrographs for both the horizontal (compare Figs. 3b and 8c) and vertical (compare Figs. 3c and 8f) specimens. Therefore, the fracture behavior of as built AlSi10Mg presents a strong correlation with the Si-rich eutectic phase orientation.

3.3.3. Fracture path

The broken notched specimens were polished until the mid-thickness plane to investigate the fracture path in relation to the melt pool microstructure. Fig. 9a presents the overall view of the fracture path in the horizontal notched specimen. Note that the melt pool profiles incorporated in Fig. 9a are extracted from the real optical micrograph and their size matches well the scale bar of this subfigure. Through meticulous observations under optical microscope (for better contrast of the melt pool border), the crack is found to propagate along only 4% of the melt pool borders between the two notches (see Supplementary Fig. S3). Therefore, the crack nearly exclusively travels across the melt pools, as their borders are more or less parallel to the loading direction (Fig. 9b-c).

Regarding the fracture path in the vertical notched specimen, the crack frequently follows the melt pool border. According to observations under optical microscope, the crack propagates along 50% of the melt pool borders between the two notches (see Supplementary Fig. S4), which is a much higher percentage than that (4%) of the horizontal specimen. Fig. 10a shows the overall fracture path and Fig. 10b highlights the local crack path overlapping one melt pool border. The two arrows in Fig. 10b indicate the start and end of the overlapping. When zooming in to reveal the correlation between the fracture and the microstructure, the crack is found to pass through the CMP (Fig. 10c) or the CMP-FMP boundary (Fig. 10d). The HAZ does not take part in the fracture process. This can be explained by the fact that the Si-rich eutectic phase of the HAZ presents a degraded connectivity (Fig. 5), thus being less prone to damage.

When observing the microstructure of the region that does not coincide with melt pool border, the crack is found to travel through the FMP, as can be seen in Fig. 10e. In such regions, damage appears simultaneously in the FMP, CMP and HAZ. Nevertheless, the damage grows more significantly in the CMP, as reflected by the extending sharp micro-cracks (see arrows in Fig. 10e).

3.3.4. Damage distribution

The study of the fracture path shows that the FMP (i.e., the microstructure constituting most of the material volume) is prone to damage whatever the orientation of the melt pool to external load. Fig. 11 presents the characteristic damage features in the FMP for both horizontal and vertical notched specimens, which show a high similarity. Damage mainly arises from the fracture of the Si-rich eutectic network and coalesces across the enclosed Al cell. As the Al cells in the FMP generally present a very small size (about 1.7 μm along the building direction and 0.3 μm in the perpendicular direction), the damage coalescence operates without significant void growth, forming oblate micro-cracks. This is more evident for the vertical notched specimen which involves an Al cell size of 0.3 μm along the crack propagation direction (see Fig. 11c-d). In this sense, larger Al cells will present a potential to delay damage coalescence.

The melt pool border can induce strain localization for vertical notched specimens owing to its lower strength compared to the FMP [8]. This has been shown in Fig. 7 and indirectly confirmed by Ben et al. [17] through higher density of geometrically necessary dislocations at the melt pool border. However, will the strain localization induce localized damage and thus significantly degrade the ductility? To answer this

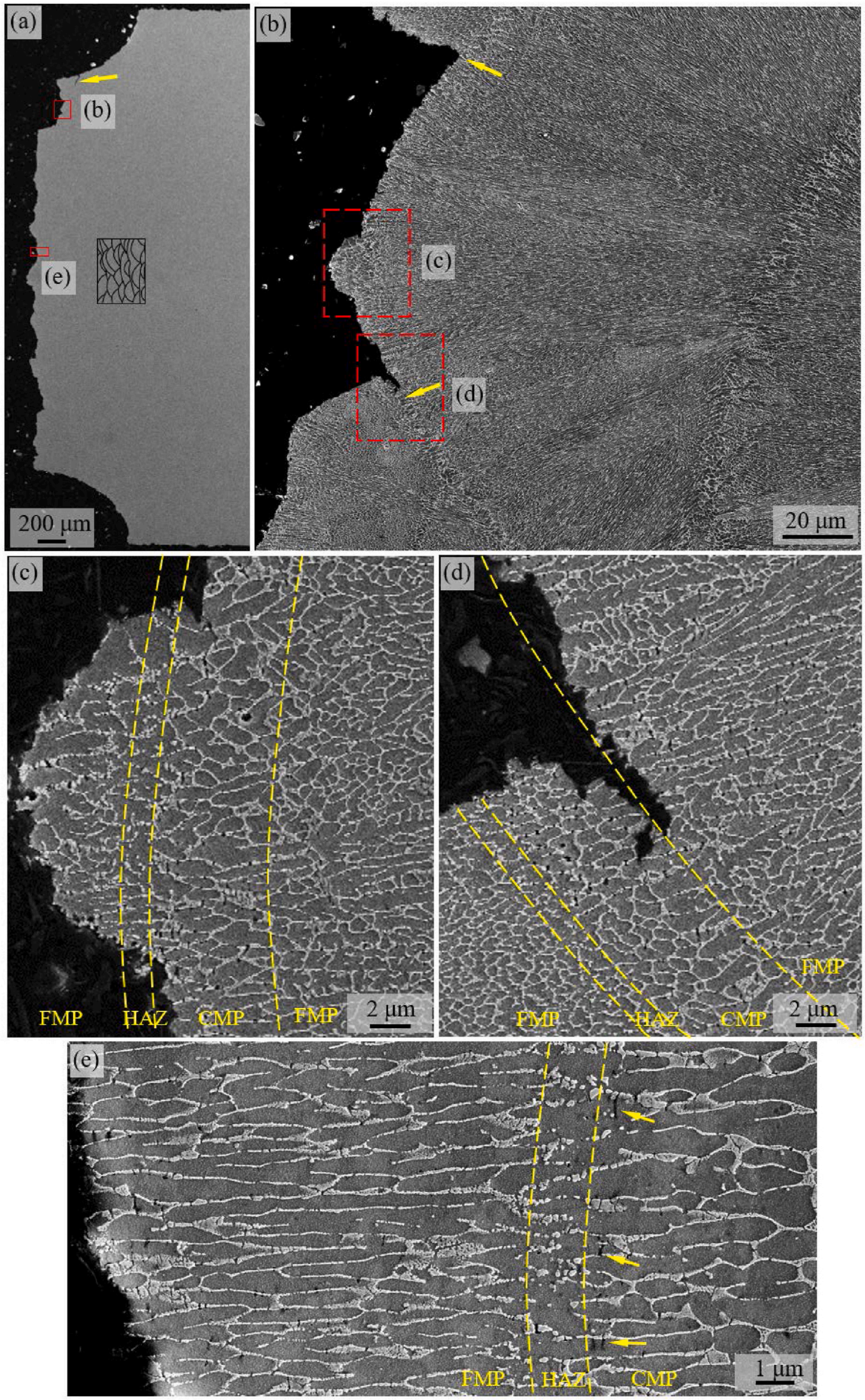

Fig. 10. Fracture path in the vertical notched specimen. Overall observation (a), fracture path along melt pool border (b), details of fracture zone at melt pool border (c) and (d), fracture path inside melt pool (e). The yellow dashed lines delimit the FMP, CMP and HAZ in (c)–(e), the two arrows in (b) indicate the start and end of the overlapping. (For interpretation of the references to color in this figure legend, the reader is referred to the Web version of this article.)

question, damage statistics in the three zones (i.e., FMP, CMP, HAZ) were obtained. A stopped secondary crack initiating from the notch (see the arrow in Fig. 10a) offers ground for this assessment. High resolution SEM micrograph (resolution of 7.4 nm) allows highlighting damage and performing distribution analysis, as presented in Fig. 12.

From the microstructure around the crack tip and wake, it is found that the crack travels through the CMP before stopping (Fig. 12a). Damage is present at both sides of the crack wake, as can be observed in Fig. 12a and b. Based on the voids extracted from the micrograph (black dots in Fig. 12b), void density distribution (Fig. 12c) and void area fraction distribution (Fig. 12d) are calculated using a subregion of 500 nm. This subregion size is selected to be able to reveal damage

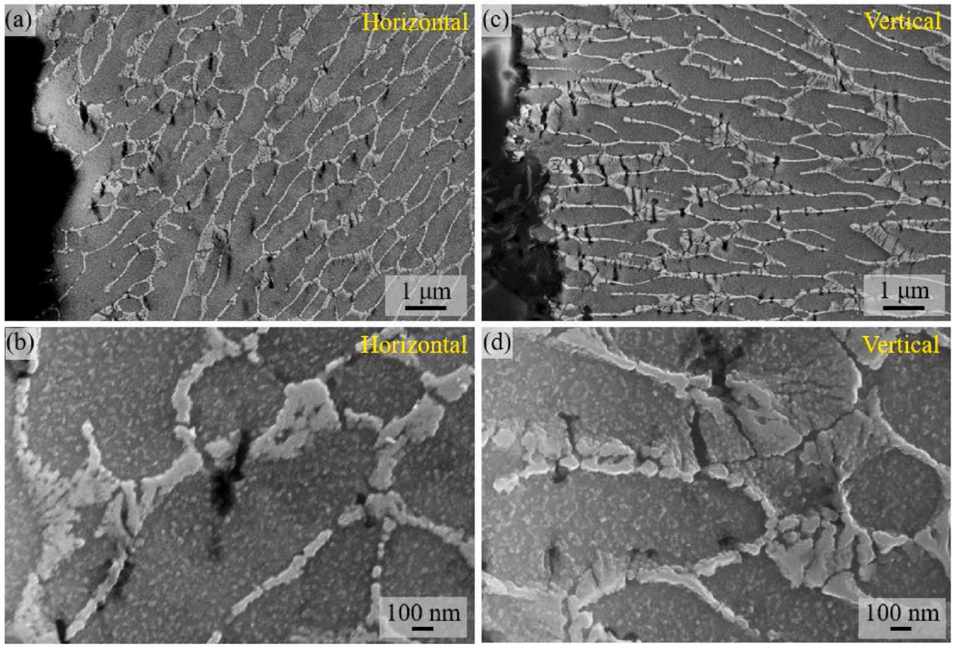

Fig. 11. Damage features in the FMP for both horizontal (a)–(b) and vertical (c)–(d) notched specimens.

distribution in the HAZ, considering its thickness of approximately 1.5 μm in the SEM micrograph. According to the distribution analysis, there is no significant difference in damage density in the FMP, CMP and HAZ (Fig. 12c). This indicates that the damage does not show signs of localization. This is in line with the 3D characterization showing that the HAZ does not present fully globularized Si particles (see Figs. 4 and 5). If we had a globularized microstructure in the HAZ, then we would have seen more localized damage and consequently low ductility of the vertical specimens. The main difference between the zones is that the CMP exhibits larger damaged area (i.e., void size, see Fig. 12d), which can be attributed to larger local strain.

From the aforementioned observations, it can be concluded that the relatively softer melt pool border does not exhibit highly localized damage. This may be due to the good strain hardening capacity of the material (see Fig. 6) which impedes the development of strain localization. The damage distribution revealed by Fig. 12 helps to understand why the ductility is not compromised in the vertical direction, as will now be extensively discussed.

4. Discussion

4.1. Microstructure

LPBF AlSi10Mg exhibits a quite complex microstructure spanning from very fine Si-rich precipitates (equivalent diameter around 10 nm) to a Si-rich eutectic network (order of magnitude of 1 μm) and melt pools (order of magnitude of 100 μm). Moreover, the Si phase exhibits high inhomogeneity in 3D morphology at the vicinity of the melt pool border (Fig. 3a), which renders microstructure characterization a challenging issue to tackle. This work has shown that 2D SEM observations do not suffice to accurately unveil the microstructure morphology. Indeed, in the HAZ, 2D SEM seems to reveal a highly globularized Si-rich phase while 3D FIB/SEM tomography shows certain level of interconnection (Fig. 4). Having the full picture of the microstructure is critical for understanding or predicting the mechanical properties, in particular the damage mechanism, as will be discussed below.

4.2. Damage and ductility

Post-mortem observation (Figs. 10 and 12) has shown that the CMP is a favored fracture path when the melt pool border is perpendicular to the tensile load (i.e., vertical specimens). Correspondingly, the crack wake region is found to exhibit higher void size in the CMP, the damage density being similar in the FMP, CMP and HAZ. This could be due to the fact that the CMP microstructure is coarser (larger enclosed Al cells, see Fig. 3a) and damage growth takes place more easily due to its lower strength.

Indeed, the microstructure of the HAZ and the CMP presents slightly lower strength compared to the FMP (roughly 11% and 5% lower, respectively, according to Ref. [8]), resulting in some strain localization in the HAZ and CMP; see Fig. 7, where the melt pool border strain localization is evidenced with yellow arrows. The Si-rich phase connectivity of the HAZ is however much lower than that of the FMP and CMP. Therefore, this region is less prone to damage nucleation. Nevertheless, it is worth noting that if the HAZ presented a fully globularized Si-rich phase, a great loss in strength would have occurred. Indeed, in our previous work [42], it has been shown that the full globularization of the Si-rich phase by heat treatment can lead to a yield strength drop by 26%. A significant loss in strength in the HAZ would have reduced overall ductility due to important strain localization, in particular in the vertical direction. The 3D characterization in Fig. 5 has revealed that the HAZ retained the “branched” type connectivity, i.e., not a full globularization like a 2D image may give as impression. We thus expect this partly retained connectivity to have as consequence only a limited strain localization in the HAZ.

The whole damage scenario for vertical specimens can be built according to the aforementioned observations as follows:

(1) Void nucleates first in the CMP due to the high connectivity of the Si-rich phase and strain localization.
(2) Then the FMP damages since the flow stress rapidly increases in the CMP owing to significant strain hardening.
(3) Damage occurs relatively late in the HAZ due to its much lower connectivity of the Si-rich phase and limited strain localization.
(4) During the damage nucleation in the FMP and HAZ, the voids continue to grow in the CMP, leading to higher damaged area.

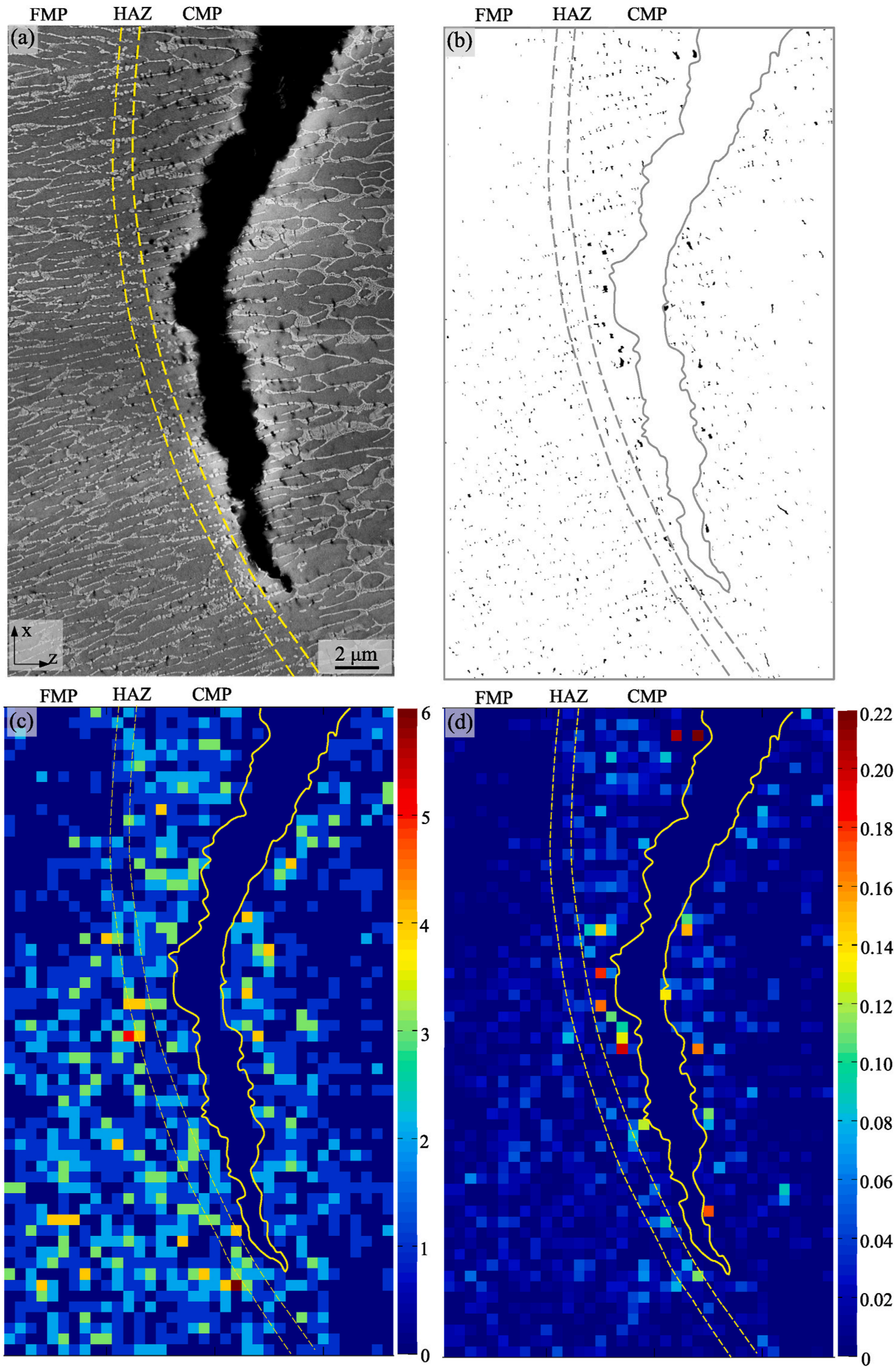

Fig. 12. Damage distribution at the vicinity of a melt pool border of a vertical notched specimen. Overall damage pattern (a), replicate of (a) highlighting the voids (b), void density distribution (number/square subregion of 500 nm) (c), void area fraction calculated within each subregion (d). The dashed lines delimit the HAZ, the solid lines delimit the crack. The loading direction coincides with the horizontal direction of the figure.

Why is the ductility not compromised although the CMP zone is slightly more prone to damage growth and significantly more solicited when loading in the vertical direction (50% of melt pool border overlapping frequency vs. 4% in horizontal direction)? It is just a question of compensation of effects. Failure of metals is controlled by damage nucleation, growth and coalescence, all three stages influencing the final strain at fracture. Coarser Si-rich network leads to lower strength and higher fracture probability in the CMP, which induce strain localization and promote void nucleation. However, larger Al phase enclosed by the Si network leaves more room for growth of voids, thus postponing their coalescence. The combined effects of relatively early nucleation, easy growth and delayed coalescence retain the material ductility. To summarize, the faster damage growth in the CMP is compensated by a later coalescence and thus the overall fracture strain is little affected even if the melt pool border is more often selected as fracture path in the vertical loading direction.

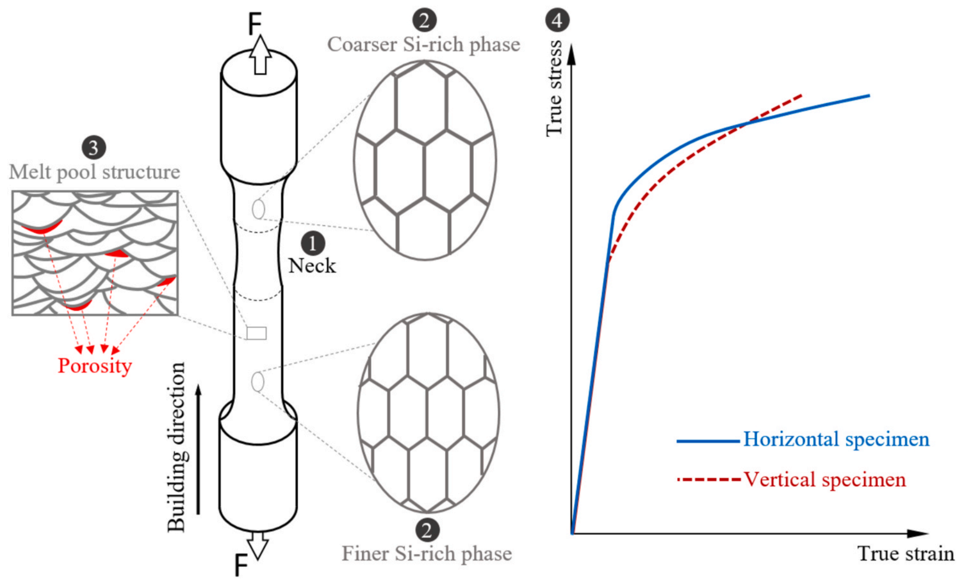

Fig. 13. Schematic addressing possible origins for lower ductility of vertical sample found in literature (Table 1).

4.3. Explanation of discrepancy between this work and literature data

Now, why is the ductility almost identical between the horizontal and vertical specimens in the present study (see Fig. 6), in contrast to previous works displayed in Table 1? There could be several reasons for the large difference reported in literature (see Fig. 13):

(1) In most of the previous studies, only engineering strain at fracture was reported, which does not represent ductility when post-necking deformation is involved, especially when the build platform is preheated, as the microstructure is coarser and the strain hardening capacity is lower, see Ref. [11]. When looking at the tensile curves in previous works, necking does occur in Refs. [16,28,29] listed in Table 1. This argument is further confirmed in our study, as the vertical specimens present post-necking deformation, their elongation is smaller than that of the horizontal specimens (Fig. 6a), but the true strain at fracture is similar between the two loading directions (Fig. 6b).
(2) Microstructure gradient has been found in long vertical specimens (gauge length of 50 mm in Ref. [31]) along the loading direction, inducing systematic strain localization toward one end of the specimen. Hitzler et al. [31] associated this microstructure gradient to a smaller ductility of vertical specimens (3.2%) compared to horizontal ones (6.5%).
(3) Some manufacturing parameters (especially low laser power) give rise to sharp lack of fusion pores along melt pool borders which promote failure of vertical specimens. A clear correlation between large pores (hundreds of micrometers) and extremely low ductility (1.7%) can be found in Ref. [22];
(4) Another factor leading to lower ductility of vertical specimens is their higher strain hardening capacity, as can be seen from tensile curves presented in previous works [26,27], which are schematized in Fig. 13. In most cases, although vertical specimens fail at lower elongation, their fracture stress is similar or higher compared to horizontal specimens (see Table 1).

It is noteworthy that there exists a case where the difference in ductility is very small (4.6% vs. 4.4% for horizontal and vertical directions, respectively) [30]. However, the tensile curves presented in that work have a very strange shape, which indicates a yield strength of 50 MPa and a failure stress of 350 MPa. The level of yield strength is not at all in line with the rest of the results reported for AlSi10Mg and thus these tensile curves should be used with caution.

The aforementioned points are not present in this work where:

(1) The ductility is assessed with true strain at fracture for both loading directions, given that the vertical specimens exhibit slight necking (see Fig. 6a). The elongation to fracture (engineering strain) is indeed found to be higher in the horizontal specimens, which do not present necking induced strain localization.
(2) The final failure occurs randomly inside the extensometer span, indicating the absence of strong microstructure gradient. This can be explained by the fact that the gauge section is relatively short (20 mm) and close to the build platform.
(3) The initial pores are generally small and present low sharpness (porosity volume fraction of 0.13%, equivalent diameter smaller than 50 μm, see our previous work [41]). The influence of such porosity on ductility is insignificant, as discussed by Zhao et al. [42].
(4) The stress level is very close in the horizontal and vertical specimens when fracture occurs (see Fig. 6b). From Fig. 6c, it can be seen that the strain hardening exponent of the vertical specimens is higher at the early stage of plastic deformation, which drives their flow stress to overtake that of the horizontal specimens, despite of lower yield strength. It then decreases rapidly and becomes smaller at a strain of approximately 5.3%. Consequently, the vertical and horizontal specimens fail at similar true stress and strain.

5. Conclusions

In the present work, the microstructure of LPBF AlSi10Mg has been characterized, with a focus on 3D Si-rich phase morphology at the melt pool border. Damage nucleation sites and fracture path have been carefully analyzed for both horizontal and vertical specimens, presenting melt pool borders parallel and perpendicular to external loading, respectively. The main conclusions are the following:

(1) 2D micrography cannot provide fully accurate characterization of the Si-rich eutectic phase, the third dimension being necessary, especially for the HAZ.
(2) The Si-rich eutectic network is degraded in the HAZ, but retains interconnection in the “branched” structure at large scale as revealed by the 3D characterization. In consequence, strain

localization in the HAZ is limited and damage can initiate in regions like the CMP and the FMP.

(3) The crack frequently propagates, but not exclusively (about 50% frequency), along the CMP band in vertical specimens. This can be explained by earlier damage nucleation and growth due to high Si-rich network connectivity and lower strength induced strain localization in the CMP.

(4) Ductility of vertical specimens is not compromised by strain localization in the CMP since the larger enclosed Al cells can postpone damage coalescence.

(5) Sound LPBF AlSi10Mg (i.e., no microstructure gradient, no large porosity) does not present any substantial damage anisotropy.

Data availability

The data that support the findings of this study are available from the corresponding author upon reasonable request.

CRediT authorship contribution statement

Lv Zhao: Conceptualization, Formal analysis, Investigation, Writing - original draft. **Juan Guillermo Santos Macías:** Formal analysis, Investigation, Writing - review & editing. **Thierry Douillard:** Investigation, Writing - review & editing. **Zhenhuan Li:** Investigation, Writing - review & editing. **Aude Simar:** Conceptualization, Funding acquisition, Writing - review & editing.

Declaration of competing interest

The authors declare that they have no known competing financial interests or personal relationships that could have appeared to influence the work reported in this paper.

Acknowledgements

The authors acknowledge the WALInnov LongLifeAM project (convention n°1810016) funded by the Service public de Wallonie Économie Emploi Recherche (SPW-EER) and the European Research Council (ERC) for the Starting Grant ALUFIX project (grant agreement n°716678). L. Zhao acknowledges the financial support from the NSFC (grant number 12002128). J. G. Santos Macías acknowledges the Fonds de la recherche scientifique - FNRS (FRIA grant), Belgium. The access to the Zeiss NVision40 FIB/SEM was provided by the CLyM (Consortium Lyon Saint-Etienne de Microscopie) supported by the CNRS, the "GrandLyon"and the Rhône-Alpes Region (France). The authors acknowledge Any-shape SA (Belgium) for the manufacturing of the LPBF AlSi10Mg samples.

Appendix A. Supplementary data

Supplementary data to this article can be found online at https://doi.org/10.1016/j.msea.2021.140845.

References

[1] J. Suryawanshi, K.G. Prashanth, S. Scudino, J. Eckert, O. Prakash, U. Ramamurty, Simultaneous enhancements of strength and toughness in an Al-12Si alloy synthesized using selective laser melting, Acta Mater. 115 (2016) 285–294.
[2] B. Chen, S.K. Moon, X. Yao, G. Bi, J. Shen, J. Umeda, K. Kondoh, Strength and strain hardening of a selective laser melted AlSi10Mg alloy, Scripta Mater. 141 (2017) 45–49.
[3] L. Girelli, M. Tocci, M. Gelfi, A. Pola, Study of heat treatment parameters for additively manufactured AlSi10Mg in comparison with corresponding cast alloy, Mater. Sci. Eng. 739 (2019) 317–328.
[4] J. Zhang, B. Song, Q. Wei, D. Bourell, Y. Shi, A review of selective laser melting of aluminum alloys: processing, microstructure, property and developing trends, J. Mater. Sci. Technol. 35 (2019) 270–284.
[5] E.O. Olakanmi, R.F. Cochrane, K.W. Dalgarno, A review on selective laser sintering/melting (SLS/SLM) of aluminium alloy powders: processing, microstructure, and properties, Prog. Mater. Sci. 74 (2015) 401–477.
[6] N. Takata, H. Kodaira, A. Suzuki, M. Kobashi, Size dependence of microstructure of AlSi10Mg alloy fabricated by selective laser melting, Mater. Char. 143 (2018) 18–26.
[7] H. Qin, V. Fallah, Q. Dong, M. Brochu, M.R. Daymond, M. Gallerneault, Solidification pattern, microstructure and texture development in Laser Powder Bed Fusion (LPBF) of Al10SiMg alloy, Mater. Char. 145 (2018) 29–38.
[8] J. Delahaye, J.T. Tchuindjang, J. Lecomte-Beckers, O. Rigo, A.M. Habraken, A. Mertens, Influence of Si precipitates on fracture mechanisms of AlSi10Mg parts processed by Selective Laser Melting, Acta Mater. 175 (2019) 160–170.
[9] Z.H. Xiong, S.L. Liu, S.F. Li, Y. Shi, Y.F. Yang, R.D.K. Misra, Role of melt pool boundary condition in determining the mechanical properties of selective laser melting AlSi10Mg alloy, Mater. Sci. Eng. 740–741 (2019) 148–156.
[10] X. Liu, C. Zhao, X. Zhou, Z. Shen, W. Liu, Microstructure of selective laser melted AlSi10Mg alloy, Mater. Des. 168 (2019) 107667.
[11] J.G. Santos Macías, T. Douillard, L. Zhao, E. Maire, G. Pyka, A. Simar, Influence on microstructure, strength and ductility of build platform temperature during laser powder bed fusion of AlSi10Mg, Acta Mater. 201 (2020) 231–243.
[12] Z. Asghar, G. Requena, E. Boller, Three-dimensional rigid multiphase networks providing high-temperature strength to cast AlSi10Cu5Ni1-2 piston alloys, Acta Mater. 59 (2011) 6420–6432.
[13] K. Bugelnig, F. Sket, H. Germann, T. Steffens, R. Koos, F. Wilde, E. Boller, G. Requena, Influence of 3D connectivity of rigid phases on damage evolution during tensile deformation of an AlSi12Cu4Ni2 piston alloy, Mater. Sci. Eng. 709 (2018) 193–202.
[14] M. Tang, P.C. Pistorius, Anisotropic mechanical behavior of AlSi10Mg parts produced by selective laser melting, JOM 69 (2017) 516–522.
[15] T. Maconachie, M. Leary, J. Zhang, A. Medvedev, A. Sarker, D. Ruan, G. Lu, O. Faruque, M. Brandt, Effect of build orientation on the quasi-static and dynamic response of SLM AlSi10Mg, Mater. Sci. Eng. 788 (2020) 139445.
[16] A. Hadadzadeh, C. Baxter, B.S. Amirkhiz, M. Mohammadi, Strengthening mechanisms in direct metal laser sintered AlSi10Mg: comparison between virgin and recycled powders, Addit. Manuf. 23 (2018) 108–120.
[17] D. Ben, Y. Ma, H. Yang, L. Meng, X. Shao, H. Liu, S. Wang, Q. Duan, Z. Zhang, Heterogeneous microstructure and voids dependence of tensile deformation in a selective laser melted AlSi10Mg alloy, Mater. Sci. Eng. 798 (2020) 140109.
[18] Z. Li, Z. Li, Z. Tan, D. Xiong, Q. Guo, Stress relaxation and the cellular structure-dependence of plastic deformation in additively manufactured AlSi10Mg alloys, Int. J. Plast. 127 (2020) 102640.
[19] D. Kim, W. Woo, J. Hwang, K. An, S. Choi, Stress partitioning behavior of an AlSi10Mg alloy produced by selective laser melting during tensile deformation using in situ neutron diffraction, J. Alloys Compd. 686 (2016) 281–286.
[20] J. Wu, X.Q. Wang, M.M. Attallah, M.H. Loretto, Microstructure and strength of selectively laser melted AlSi10Mg, Acta Mater. 117 (2016) 311–320.
[21] A. Pineau, A.A. Benzerga, T. Pardoen, Failure of metals I: brittle and ductile fracture, Acta Mater. 107 (2016) 424–483.
[22] U. Tradowsky, J. White, R.M. Ward, N. Read, W. Reimers, M.M. Attallah, Selective laser melting of AlSi10Mg: influence of post-processing on the microstructural and tensile properties development, Mater. Des. 105 (2016) 212–222.
[23] J.C. Hastie, M.E. Kartal, L.N. Carter, M.M. Attallah, D.M. Mulvihill, Classifying shape of internal pores within AlSi10Mg alloy manufactured by laser powder bed fusion using 3D X-ray micro computed tomography: influence of processing parameters and heat treatment, Mater. Char. 163 (2020) 110225.
[24] T. Hirata, T. Kimura, T. Nakamoto, Effects of hot isostatic pressing and internal porosity on the performance of selective laser melted AlSi10Mg alloys, Mater. Sci. Eng. 772 (2020) 138713.
[25] D. Buchbinder, W. Meiners, K. Wissenbach, R. Poprawe, Selective laser melting of aluminum die-cast alloy–correlations between process parameters, solidification conditions, and resulting mechanical properties, J. Laser Appl. 27 (2015) S29205.
[26] N. Takata, H. Kodaira, K. Sekizawa, A. Suzuki, M. Kobashi, Change in microstructure of selectively laser melted AlSi10Mg alloy with heat treatments, Mater. Sci. Eng. 704 (2017) 218–228.
[27] J. Fiocchi, C. Biffi, C. Colombo, L. Vergani, A. Tuissi, Ad hoc heat treatments for selective laser melted AlSi10Mg alloy aimed at stress-relieving and enhancing mechanical performances, JOM 72 (2020) 1118–1127.
[28] E. Padovano, C. Badini, A. Pantarelli, F. Gili, F. D'Aiuto, A comparative study of the effects of thermal treatments on AlSi10Mg produced by laser powder bed fusion, J. Alloys Compd. 831 (2020) 154822.
[29] R. Casati, M. Nasab, M. Coduri, V. Tirelli, M. Vedani, Effects of platform preheating and thermal-treatment strategies on properties of AlSi10Mg alloy processed by selective laser melting, Metals 8 (2018) 954.
[30] S.R. Ch, A. Raja, P. Nadig, R. Jayaganthan, N.J. Vasa, Influence of working environment and built orientation on the tensile properties of selective laser melted AlSi10Mg alloy, Mater. Sci. Eng. 750 (2019) 141–151.
[31] L. Hitzler, C. Janousch, J. Schanz, M. Merkel, B. Heine, F. Mack, W. Hall, A. Öchsner, Direction and location dependency of selective laser melted AlSi10Mg specimens, J. Mater. Process. Technol. 243 (2017) 48–61.
[32] E. Sert, L. Hitzler, S. Hafenstein, M. Merkel, E. Werner, A. Öchsner, Tensile and compressive behaviour of additively manufactured AlSi10Mg samples, Progress Addit. Manuf. 5 (2020) 305–313.
[33] Q. Tan, J. Zhang, N. Mo, Z. Fan, Y. Yin, M. Bermingham, Y. Liu, H. Huang, M. Zhang, A novel method to 3D-print fine-grained AlSi10Mg alloy with isotropic properties via inoculation with LaB6 nanoparticles, Addit. Manuf. 32 (2020) 101304.

[34] L.F. Wang, J. Sun, X.L. Yu, Y. Shi, X.G. Zhu, L.Y. Cheng, H.H. Liang, B. Yan, L. J. Guo, Enhancement in mechanical properties of selectively laser melted AlSi10Mg aluminum alloys by T6-like heat treatment, Mater. Sci. Eng. 734 (2018) 299–310.
[35] I. Rosenthal, R. Shneck, A. Stern, Heat treatment effect on the mechanical properties and fracture mechanism in AlSi10Mg fabricated by additive manufacturing selective laser melting process, Mater. Sci. Eng. 729 (2018) 310–322.
[36] K. Kempen, L. Thijs, J. Van Humbeeck, J.-P. Kruth, Mechanical properties of AlSi10Mg produced by selective laser melting, Phys. Procedia 39 (2012) 439–446.
[37] Y.J. Liu, Z. Liu, Y. Jiang, G.W. Wang, Y. Yang, L.C. Zhang, Gradient in microstructure and mechanical property of selective laser melted AlSi10Mg, J. Alloys Compd. 735 (2018) 1414–1421.
[38] R. Everett, M. Duffy, S. Storck, M. Zupan, A variogram analysis of build height effects in an additively manufactured AlSi10Mg part, Addit. Manuf. 35 (2020) 101306.
[39] I. Maskery, N. Aboulkhair, M. Corfield, C. Tuck, A. Clare, R. Leach, R. Wildman, I. Ashcroft, R. Hague, Quantification and characterisation of porosity in selectively laser melted Al-Si10-Mg using X-ray computed tomography, Mater. Char. 111 (2016) 193–204.
[40] EOS GmbH - Electro Optical Systems, Material Data Sheet for EOS Aluminium AlSi10Mg, München, 2014.
[41] J.G. Santos Macías, C. Elangeswaran, L. Zhao, B. Van Hooreweder, J. Adrien, E. Maire, J.Y. Buffière, W. Ludwig, P.J. Jacques, A. Simar, Ductilisation and fatigue life enhancement of selective laser melted AlSi10Mg by friction stir processing, Scripta Mater. 170 (2019) 124–128.
[42] L. Zhao, J.G. Santos Macías, L. Ding, H. Idrissi, A. Simar, Damage mechanisms in selective laser melted AlSi10Mg under as built and different post-treatment conditions, Mater. Sci. Eng. 764 (2019) 138210.